(Supporting Information)

Synergistic ion-electron coupling in thermoelectric hydrogels for self-powered sensing

Chuke Zhao [a,1], Bangzhou Tian [a,1], Zijian Lin [a], Ding Ren [a], Qiang Sun [b,c], Ran Ang [a,d,e,*]

[a] *Key Laboratory of Radiation Physics and Technology, Ministry of Education, Institute of Nuclear Science and Technology, Sichuan University, Chengdu, Sichuan 610064, China*

[b] *State Key Laboratory of Oral Diseases, National Center for Stomatology, National Clinical Research Center for Oral Diseases, West China Hospital of Stomatology, Sichuan University, Chengdu, Sichuan 610041, China*

[c] *Sichuan Provincial Engineering Research Center of Oral Biomaterials, Chengdu, Sichuan 610041, China*

[d] *College of Physics, Sichuan University, Chengdu 610064, China*

[e] *Institute of New Energy and Low-Carbon Technology, Sichuan University, Chengdu 610065, China*

[1] These authors contribute equally to this work.

[*] Corresponding authors.

E-mail addresses: rang@scu.edu.cn (R.A.)

Note S1. Quantitative analysis in ion–electron coupled thermoelectric systems.[1]

Consider a homogeneous hydrogel containing both anions/cations and electrons/holes. Under equilibrium conditions (no temperature gradient), all charge carriers are uniformly distributed, and no net current is generated. When a temperature gradient is applied across the hydrogel, thermal diffusion drives ions from the hot side to the cold side, producing an ionic diffusion current (expressed as J_{Diff}) in the circuit. Simultaneously, the electronic thermoelectric effect contributes an electron current (expressed as J_{e-TE}). As charge carriers directionally migrate, charge accumulates at the two ends of the hydrogel, establishing a built-in electric field opposite to the direction of diffusion. This field induces a drift current (expressed as J_{Drift}) that opposes the diffusion current.

Under open-circuit conditions at equilibrium, the thermal diffusion currents of electrons/holes and ions are precisely counterbalanced by the opposing drift currents, yielding zero net current:

$$J_{Diff} + J_{e-Te} - J_{Drift} = 0$$

Among them, the J_{Diff} can be derived from the Fick's law:

$$J_{Diff} = \sum \left[q z_i D_i \frac{dC_i}{dx} \right]$$

Expressing it in terms of anions and cations, it can be written as:

$$J_{Diff} = q\left(D_+ z_+ \frac{dC_+}{dx} - D_- z_- \frac{dC_-}{dx} \right)$$

Where q is the charge, D is the diffusion coefficient, z is the number of charges per ion, and C is the ion concentration.

The reverse drift current J_{Drift} can be derived from the Ohm's law:

$$J_{Drift} = nq\mu \cdot E$$

$$\sigma = nq\mu$$

$$J_{Drift} = \sigma \cdot E = \sigma \cdot \frac{dV}{dx}$$

Where n is the carrier density, μ is the carrier mobility, σ is the electrical conductivity, and E is the electric field intensity.

The current $J_{e\text{-}Te}$ arising from the electronic thermoelectric effect is given by the Seebeck coefficient as:

$$J_{e-TE} = \frac{S_e \Delta T}{R}$$

Where R is the resistance, and ΔT is the temperature gradient.

Substituting the expressions for J_{Diff}, J_{e-TE} and J_{Drift} into the equation yields:

$$qA\left(D_+ z_+ \frac{dC_+}{dx} - D_- z_- \frac{dC_-}{dx}\right) + \frac{S_e \Delta T}{R} - \sigma A \frac{dV}{dx} = 0$$

This simplifies to:

$$\frac{dV}{dx} = \frac{q}{\sigma}\left(D_+ z_+ \frac{dC_+}{dx} - D_- z_- \frac{dC_-}{dx}\right) + \frac{S_e \Delta T}{R\sigma A}$$

When we define macroscopically, it can be written as:

$$\frac{\Delta V}{\Delta x} = \frac{q}{\sigma}\left(D_+ z_+ \frac{\Delta C_+}{\Delta x} - D_- z_- \frac{\Delta C_-}{\Delta x}\right) + \frac{S_e \Delta T}{R\sigma A}$$

Substituting the expression for R gives:

$$R = \frac{L}{\sigma S} = \frac{\Delta x}{\sigma_e A}$$

$$\frac{\Delta V}{\Delta x} = \frac{q}{\sigma}\left(D_+ z_+ \frac{\Delta C_+}{\Delta x} - D_- z_- \frac{\Delta C_-}{\Delta x}\right) + \frac{S_e \Delta T}{\Delta x} \cdot \frac{\sigma_e}{\sigma}$$

$$\Delta V = \frac{q}{\sigma}\left(D_+ z_+ \Delta C_+ - D_- z_- \Delta C_-\right) + S_e \Delta T \cdot \frac{\sigma_e}{\sigma}$$

According to the Soret effect for ion diffusion under temperature gradients, the current density generated by the mobile ions is given by:

$$J = -D\Delta C - D_T C \Delta T$$

Where D_T is thermodiffusion coefficient.

Under equilibrium conditions, the charges generated by ion migration cancel each other out, resulting in $J = 0$, therefore:

$$\Delta C = - C S_T \Delta T$$

Where $S_T = D_T / D$ is the Soret coefficient.

Substituting this into the equation, and noting that the charge numbers of the anions and cations are equal (both taken as 1), yields:

$$\Delta V = \frac{q}{\sigma}\left(D_- C_- S_{T-} \Delta T - D_+ C_+ S_{T+} \Delta T\right) + S_e \Delta T \cdot \frac{\sigma_e}{\sigma}$$

Thus, the Seebeck coefficient (*S*) in the ion–electron coupled thermoelectric system can be expressed as:

$$S = \frac{\Delta V}{\Delta T} = \frac{q}{\sigma}\left(D_- C_- S_{T-} - D_+ C_+ S_{T+}\right) + \frac{\sigma_e}{\sigma} S_e$$

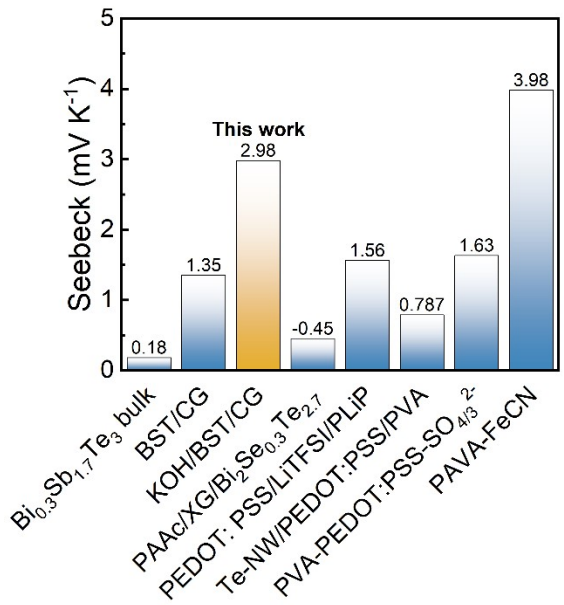

Figure S1. Comparison of Seebeck coefficients with related materials.[2–6]

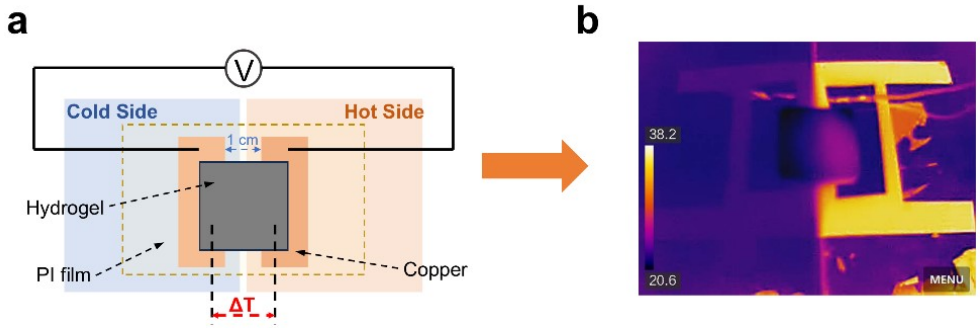

Figure S2. Schematic illustration of the experimental procedure for evaluating the thermoelectric properties of hydrogels. (a) Schematic of the thermoelectric measurement setup. (b) Representative infrared thermal image acquired during Seebeck coefficient measurements, illustrating the establishment of a stable temperature gradient across the hydrogel.

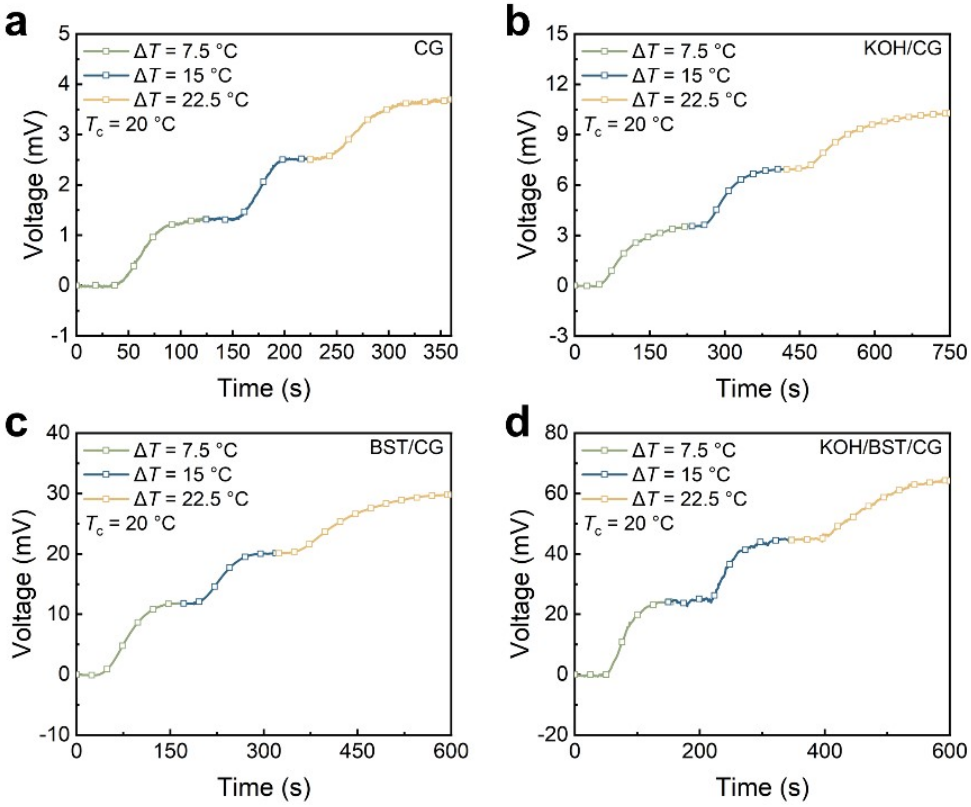

Figure S3. Comparative thermoelectric voltage responses of CG-based hydrogels under an identical applied temperature gradient. **(**a) CG hydrogel. (b) KOH/CG hydrogel. (c) BST/CG hydrogel. (d) KOH/BST/CG hydrogel.

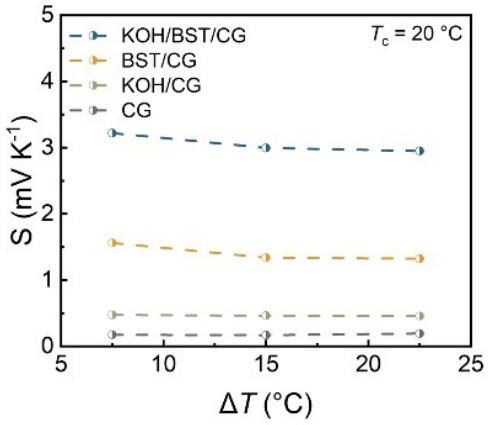

Figure S4. Seebeck coefficient of CG-based hydrogels measured under different applied temperature gradients. The hydrogels exhibit a stable and linear voltage-temperature relationship within the room-temperature range, indicating their suitability for quantitative thermoelectric sensing applications.

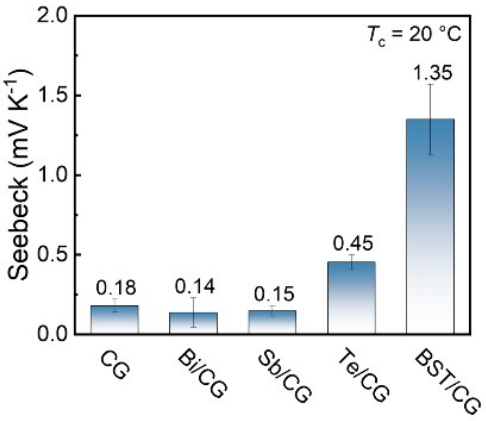

Figure S5. Seebeck coefficient of CG-based hydrogels incorporating different conductive fillers. Despite the comparable electrical conductivity of all fillers, only Te and BST lead to a pronounced enhancement of the Seebeck coefficient, which can be attributed to their intrinsic thermoelectric characteristics.

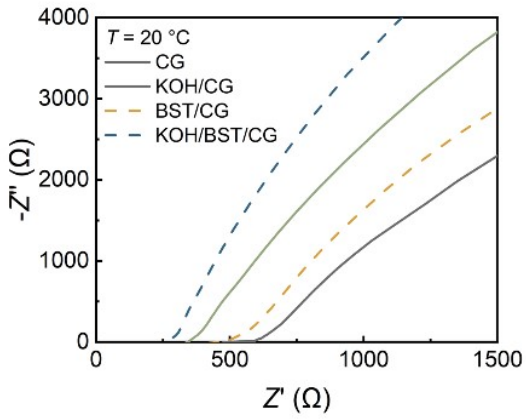

Figure S6. Electrochemical impedance spectra of CG-based hydrogels. The ionic resistance (R) is determined from the intercept of the semicircular curve with the real axis, and the ionic conductivity (σ_i) is calculated according to $\sigma_i = L / (R \times S)$, where L is the hydrogel thickness, S is the cross-sectional area, and R is the measured ionic resistance.

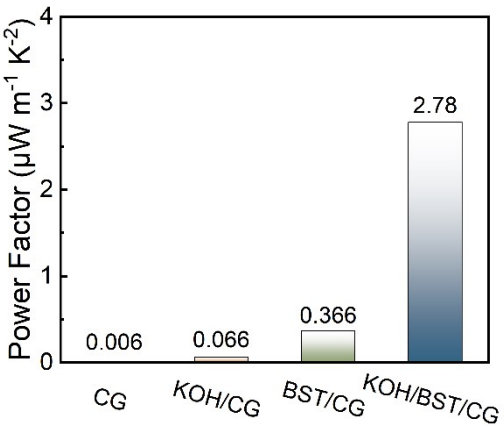

Figure S7. Power factor of the CG-based hydrogels.

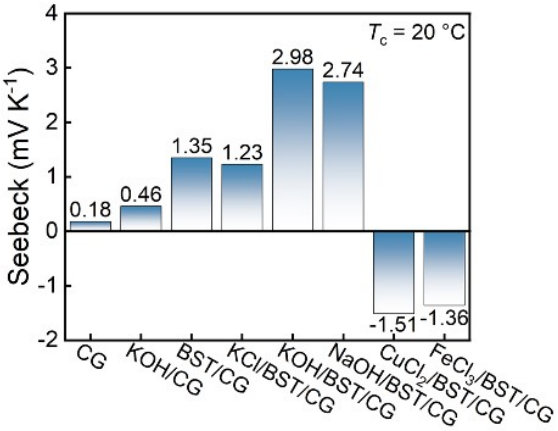

Figure S8. Seebeck coefficient of BST/CG hydrogels with different introduced ions. Among the tested ionic solutions, KOH and NaOH are basic, KCl is neutral, and $CuCl_2$ and $FeCl_3$ are acidic, highlighting the influence of ion type and solution pH on the thermoelectric response.

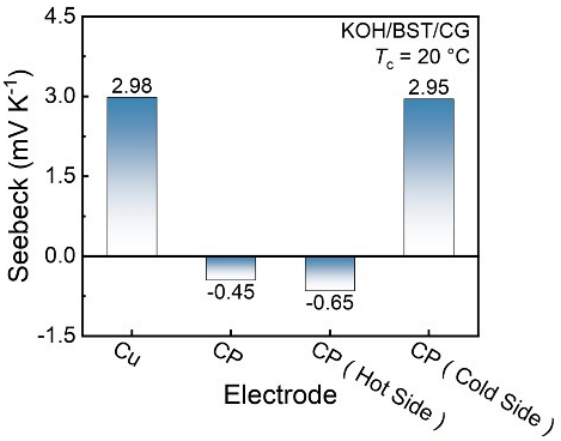

Figure S9. Influence of different electrodes on the Seebeck coefficient of KOH/BST/CG hydrogels. Replacing the electrode with carbon paper (CP) significantly alters the thermoelectric response, even reversing the Seebeck coefficient. The electrode effect is confined to the heated side, indicating that the hydrogel's thermoelectric behavior is primarily determined by the temperature-controlled electrode interface. These results provide guidance for the design and interpretation of subsequent infrared laser irradiation experiments.

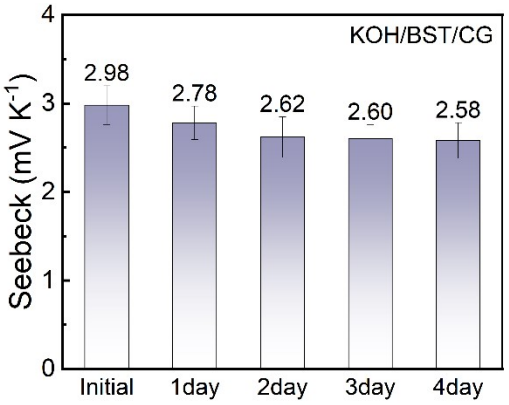

Figure S10. Long-term stability of the Seebeck coefficient of the KOH/BST/CG hydrogel during storage at 20℃ after encapsulation.

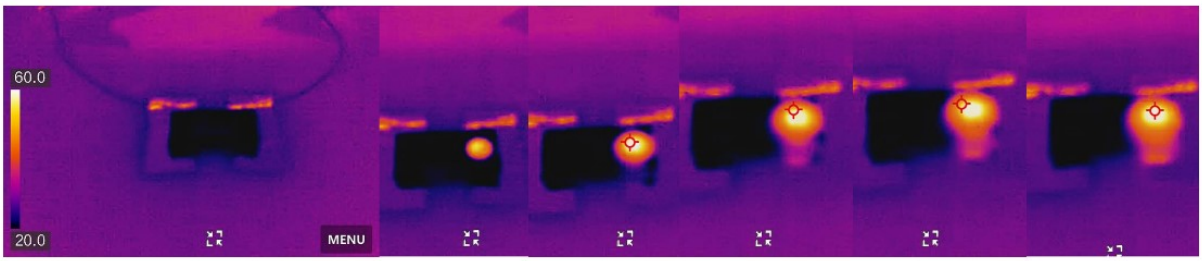

Figure S11. Infrared Thermal image of KOH/BST/CG hydrogel under near-infrared (NIR) irradiation. The image illustrates the formation of a temperature gradient across the hydrogel, with a larger gradient between the irradiated (top) surface and the bottom compared to the gradient between the underside and the cold-side interface.

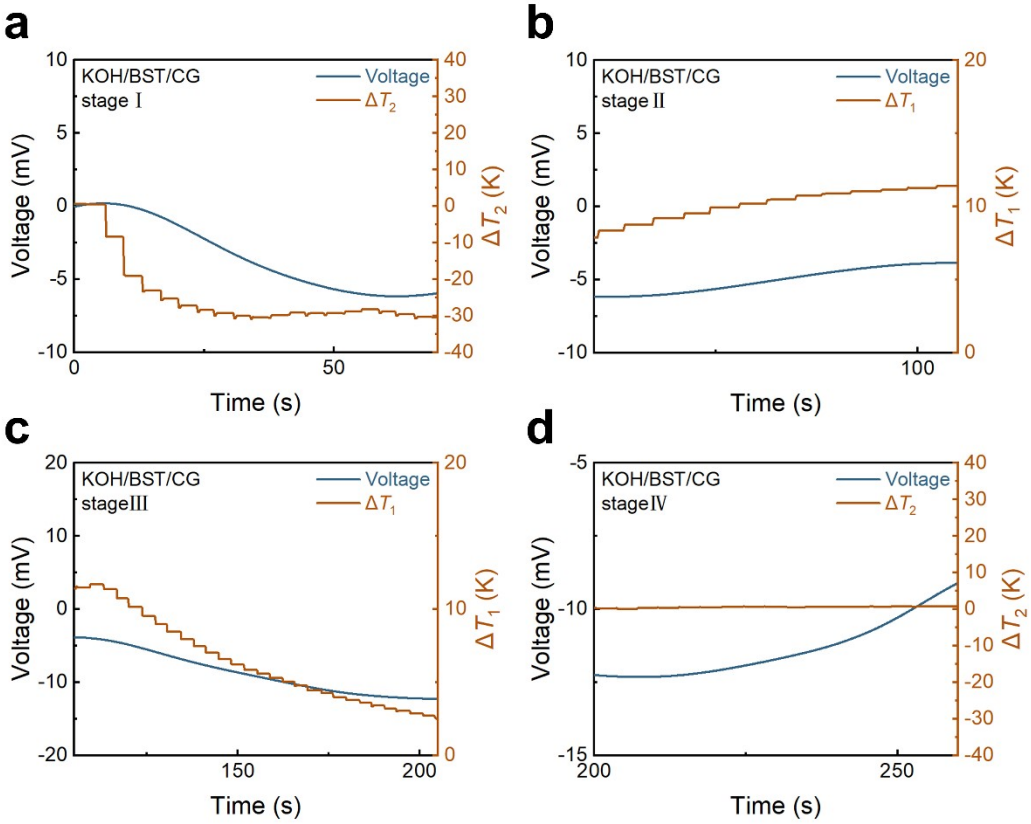

Figure S12. Staged voltage response of the KOH/BST/CG hydrogel under NIR irradiation. In Stage I, the voltage response is dominated by ΔT_2. During the equilibration process, it gradually transitions to the intrinsic ΔT_1 in Stage II. After the laser is turned off, the voltage response first decreases in Stage III due to the reduction in ΔT_1, and then rises in Stage IV driven by the approach to steady state, eventually tending toward zero.

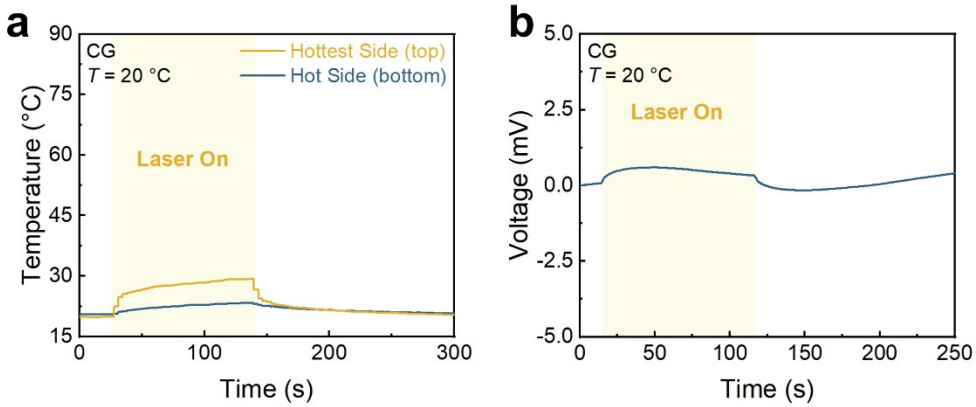

Figure S13. Temperature and voltage responses of CG hydrogel matrix under NIR irradiation. (a) Temperature evolution of the hydrogel. (b) Corresponding voltage response. Due to the optical transparency of the CG matrix and its low NIR absorption, both the temperature rise and thermoelectric voltage generation are minimal.

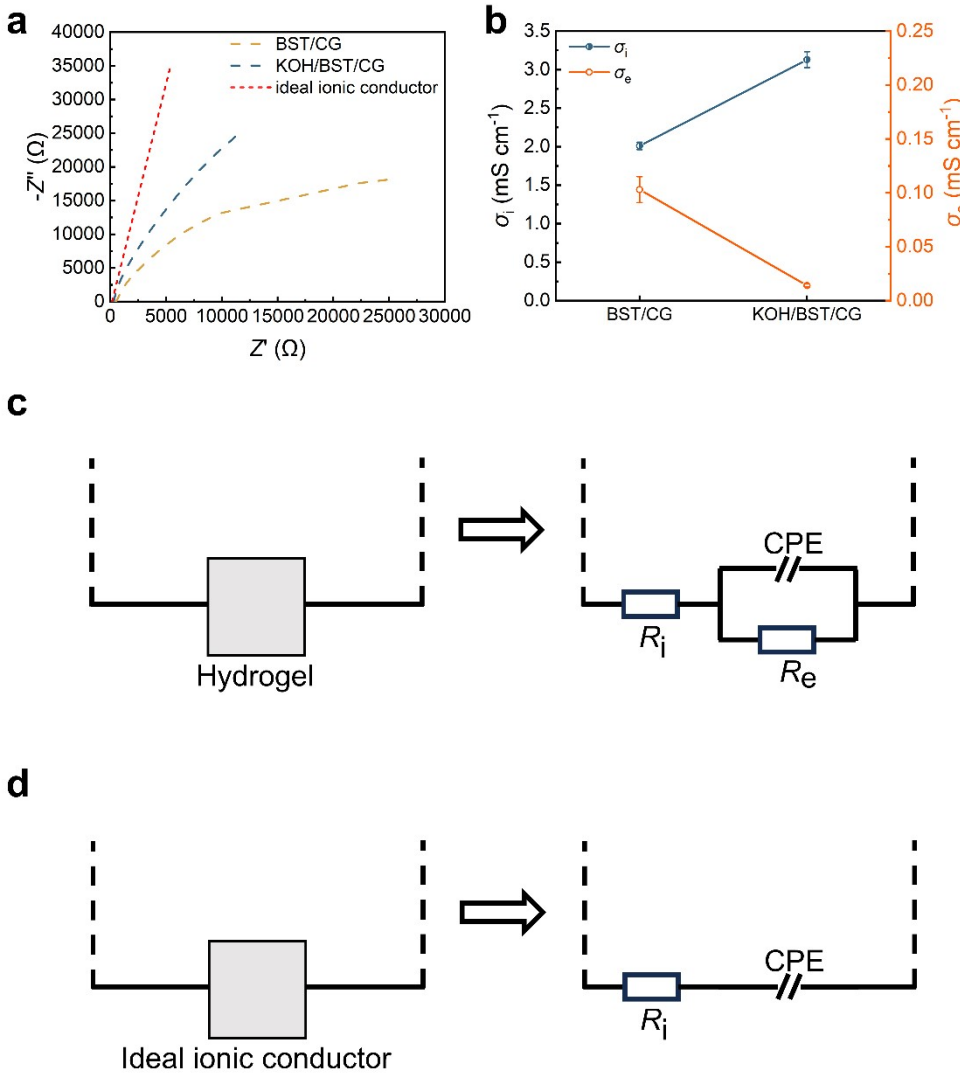

Figure S14. Effect of KOH incorporation on the conduction mechanism of KOH/BST/CG hydrogels, shifting the behavior toward ion-dominated transport. (a) Nyquist plots of KOH/BST/CG and BST/CG hydrogels. (b) Comparison of electronic and ionic conductivities before and after KOH addition. (c) Randles equivalent circuit representing the hydrogel. (d) Randles equivalent circuit of an ideal ionic conductor.

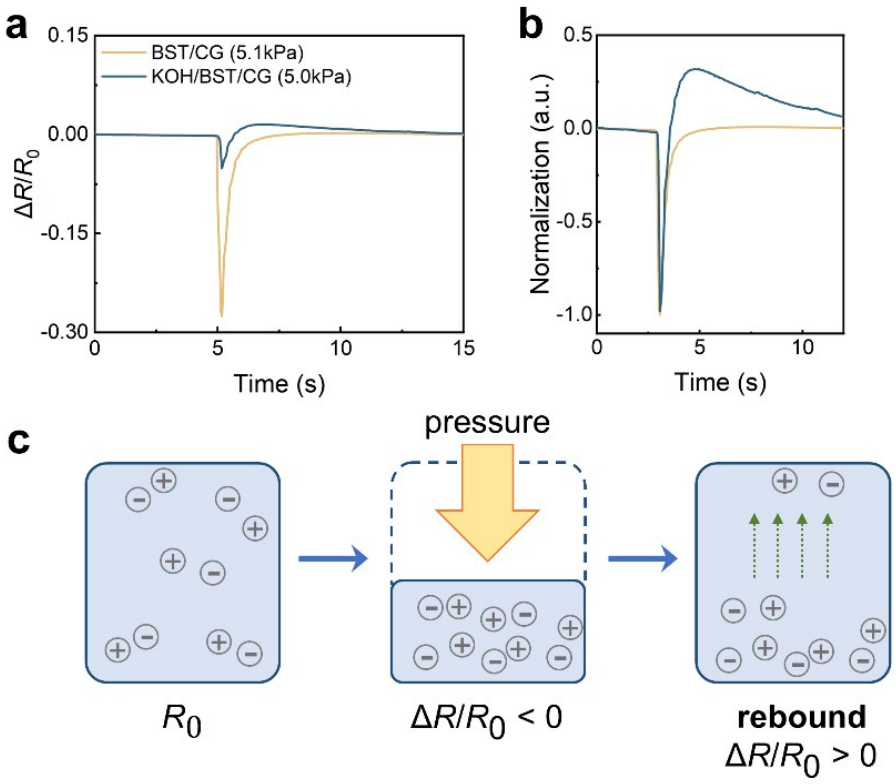

Figure S15. Piezoresistive behavior of BST/CG and KOH/BST/CG hydrogels. (a) Relative resistance change ($\Delta R/R_0$) under cyclic pressure (~5 kPa). (b) Normalized resistance responses, showing a pronounced rebound for the KOH/BST/CG hydrogel upon pressure release. (c) Schematic illustration of the proposed ion-dominated conduction mechanism in KOH/BST/CG under applied pressure.

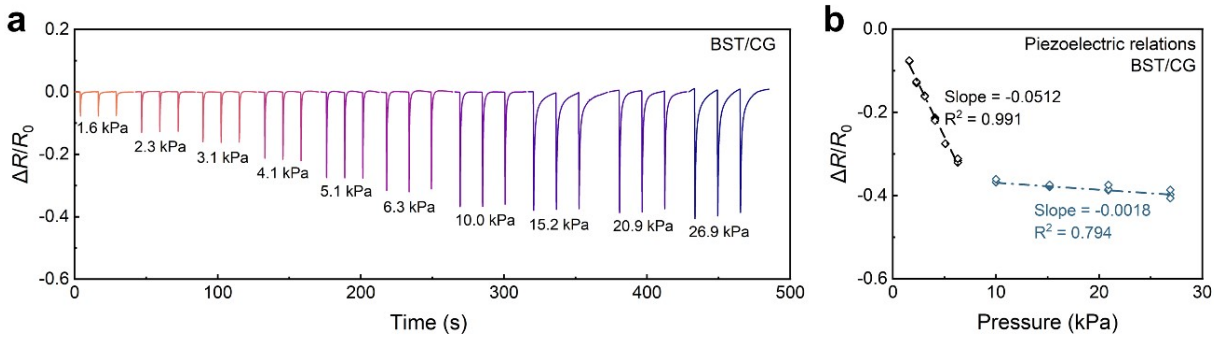

Figure S16. Piezoresistive properties of BST/CG hydrogel. (a) Relative resistance response under cyclic compressive loading. (b) Dependence of resistance on applied pressure, showing a linear relationship.

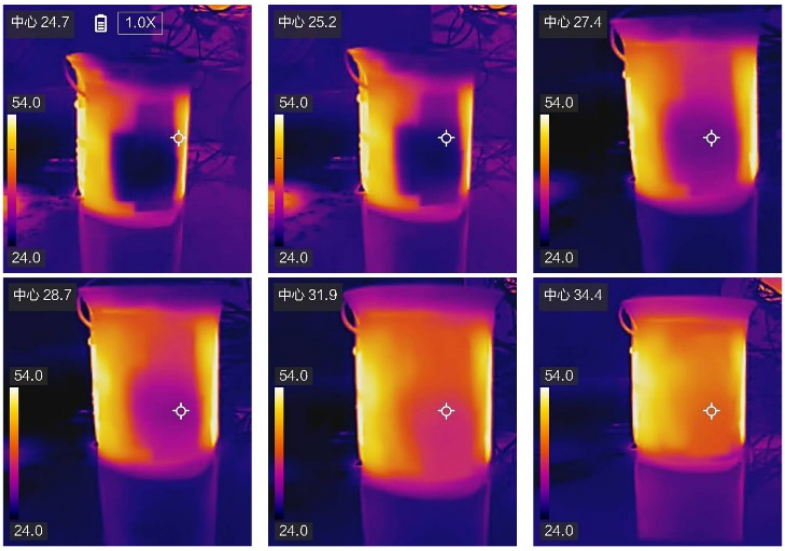

Figure S17. Infrared thermal images of KOH/BST/CG hydrogel used in a water-temperature sensing experiment. The images illustrate the formation of a temperature gradient across the hydrogel upon water addition.

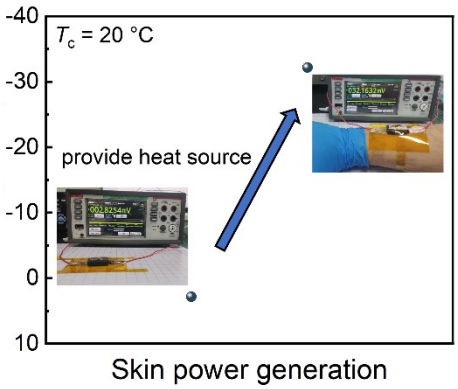

Figure S18. Voltage generation by KOH/BST/CG hydrogel at room temperature, utilizing the temperature gradient between the forearm and ambient air. This demonstration highlights the hydrogel's potential as a wearable thermoelectric generator.

Table S1. Thermoelectric properties of doped materials and the matrix at room temperature.

Materials	**thermoelectric mechanisms**	**Electronic conductivity (σ) (S m^{-1})**	**Seebeck (S) (mV K^{-1})**	**Thermal conductivity (κ) (W m^{-1} K^{-1})**	**zT**
BST bulk	Seebeck effect	0.9×10^5	0.18	1.1	~0.79
Bi bulk	Seebeck effect	1×10^6	-0.07	8	~0.18
Sb bulk	Seebeck effect	2.4×10^6	0.047	24.3	~0.07
Te bulk	Seebeck effect	1×10^5	0.14	2.2	~0.27
CG hydrogel	Soret effect	0.01	0.18	/	/

Table S2. Comparison of thermoelectric properties with other reported ion-electron coupled hydrogels.

Materials	***S*** **(mV K^{-1})**	***σ*** **(mS cm^{-1})**	**Normalized power densities (μW m^{-2} K^{-2})**	**Refs.**
$CuCl_2$/MXene/PVA	-3.13	12.7	8.89	[7]
PVA-PEDOT:PSS-$SO_{4/3}^{2-}$	1.63	29.2	0.288	[2]
PEDOT:PSS/LiTFSI/PLiP	1.56	350	/	[5]
Te-NWs/PEDOR:PSS/PVA	0.79	11	0.037	[3]
PAAc/XG/$Bi_2Se_{0.3}Te_{2.7}$	-0.45	43	0.026	[4]
KOH/BST/CG	**2.98**	**3.13**	**0.079**	**This work**

References

1 Y. He, S. Li, R. Chen, X. Liu, G. O. Odunmbaku, W. Fang, X. Lin, Z. Ou, Q. Gou, J. Wang, N. A. N. Ouedraogo, J. Li, M. Li, C. Li, Y. Zheng, S. Chen, Y. Zhou and K. Sun, *Nano-Micro Lett.*, 2023, **15**, 101.

2 C. Tian, C. Bai, T. Wang, Z. Yan, Z. Zhang, K. Zhuo and H. Zhang, *Nano Energy*, 2023, **106**, 108077.

3 S. Kong, Z. Huang, Y. Hu, Y. Jiang, Y. Lu, W. Zhao, Q. Shi, M. Yuan, B. Dai, J. Li, W. J. Yang and Y. Xie, *Nano Energy*, 2023, **115**, 108708.

4 J. Li, T. Xu, Z. Ma, W. Li, Y. Qian, Y. Tao, Y. Wei, Q. Jiang, Y. Luo and J. Yang, *ENERGY Environ. Mater.*, 2024, **7**, e12547.

5 X. Jing, W. He, S. Hua, S. Xia and G. Gao, *Chem. Eng. J.*, 2026, **530**, 173389.

6 Y. Tian, W. Wei, Z. Sun, Y. Hu, K. Li, Q. Zhang, Y. Li, C. Hou and H. Wang, *Adv. Funct. Mater.*, 2025, **35**, 2417740.

7 D. Ji, B. Li, D. Zhang, B. T. Raj, M. Rezeq, W. Cantwell and L. Zheng, *Small*, 2025, **21**, 2407529.